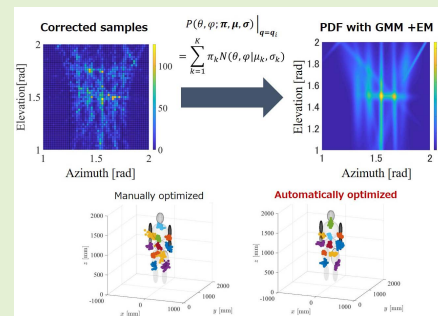


# Gaussian Mixture Model Parameter Optimization in Range Points Migration-Based Three-Dimensional Radar Imaging

Tomoki Ohmori, Shuto Takahashi, and Shouhei Kidera<sup>1b</sup>, *Member, IEEE*

**Abstract**—Millimeter-wave (MMW) imaging radar is one of the major environmental sensors in recent self-driving or driver assistance systems and provides environmentally robust sensing even in optically challenging conditions. As a promising three-dimensional (3-D) radar imaging technique, this study focuses on the range points migration (RPM) method, which has advantages in terms of accuracy and low complexity. In the original RPM algorithm, the parameters are manually or empirically determined by considering the sensor configuration and target shape or distance. To address this limitation, we introduced a novel parameter optimization scheme based on the Gaussian mixture model (GMM) and the expectation maximization (EM) algorithm. In addition, we used the  $k$ -space decomposition-based parameter determination scheme to determine target shape-dependent parameter selection. The results, assuming the human body imaging scenario, showed that our proposed method retains a highly accurate target image without requiring empirical parameter selection.

**Index Terms**—Three-dimensional imaging radar, synthetic aperture radar, range points migration (RPM), Gaussian mixture model (GMM), expectation maximization (EM) algorithm.



## I. INTRODUCTION

ADVANCED sensors requiring a highly accurate three-dimensional (3-D) environmental monitoring are highly demanded in driver assistance or self-driving systems, such as for automatic parking or pedestrian collision avoidance. The microwave or millimeter-wave (MMW) imaging radar is regarded as an indispensable sensing technique for environmental sensing, which can be applied in the presence of optically challenging conditions, such as dense fog, bad weather, or strong backlight. Many studies have been conducted to apply MMW imaging radar to

applications such as human recognition [1]–[4], or human body screening [5], [6].

Major imaging approaches for the above short-range radar applications are based on coherent integration-based methods, such as synthetic aperture radar (SAR) [7], Kirchhoff migration [8], [9], or range migration algorithm [6], [10], [11], through which a higher azimuth resolution is achieved in a higher-frequency signal. Nonetheless, these methods require sufficiently small intervals of array configuration or observation points for satisfying the Nyquist criteria to avoid an ambiguous response due to phase uncertainty. The sparse regularization scheme known as compressed sensing (CS) is one of the solutions to the above problem [12], [13]; however, it has a large computational cost. In addition, the coherent integration-based method requires an expensive computation cost to get a fully volumetric image with a small pixel size, which is preliminarily allocated as a region of interest (ROI), including all target areas. The acceleration scheme such as F-k interpolation [14], [15] has been developed, there is an inherent problem how to determine the ROI area without prior knowledge of target location or shape.

On the contrary, the incoherent mapping-based radar imaging method has been recently developed, where the discrete points on the range profile associated with sensor location, known as the range points, are solely converted to their reflection points on the target boundary. Range points

Manuscript received February 24, 2021; revised March 24, 2021; accepted March 26, 2021. Date of publication March 31, 2021; date of current version June 14, 2021. This work was supported by Japan Science and Technology Agency, Precursory Research for Embryonic Science and Technology (JST PRESTO), Japan, under Grant JPMJPR1771. The associate editor coordinating the review of this article and approving it for publication was Dr. Michail Antoniou. (*Corresponding author: Shouhei Kidera.*)

Tomoki Ohmori and Shuto Takahashi are with the Graduate School of Informatics and Engineering, The University of Electro-Communications, Chofu 182-8585, Japan.

Shouhei Kidera is with the Graduate School of Informatics and Engineering, The University of Electro-Communications, Chofu 182-8585, Japan, and also with the Japan Science and Technology Agency (JST), Precursory Research for Embryonic Science and Technology (PRESTO), Chiyoda 102-0076, Japan (e-mail: kidera@uec.ac.jp).

Digital Object Identifier 10.1109/JSEN.2021.3070022

1558-1748 © 2021 IEEE. Personal use is permitted, but republication/redistribution requires IEEE permission.

See <https://www.ieee.org/publications/rights/index.html> for more information.

migration (RPM) [16] is one of these types of methods and offers accurate, high-speed conversion from the range point to the reflection point by the weighted kernel density estimator. Notably, the RPM does not require prior connection or tracking, even when multiple range points at the same sensor locations are observed. The effectiveness of the RPM have been widely demonstrated, assuming the actual human body imaging with various frequency band radars [17]–[20]. However, the reconstruction accuracy in RPM, that determines the correlation length of the kernel-based weighting function, depends on selected parameters. These parameters must be changed according to the sensor configuration, target location or structure, which are usually unknown in most cases. Here, to determine hyper parameters, we introduce the Gaussian mixture model (GMM)-based parameter optimization using the Bayesian framework, particularly via expectation maximization (EM) algorithm [22], that have been partially introduced in [21]. As a significant contribution from the literature [21], the  $k$ -space decomposition scheme [23] is introduced in the RPM processing to enhance the accuracy and processing speed, and the correlation length along the sensor direction is automatically determined by the responses of  $k$ -space, denoting the dominant scattering area of the illuminated target surface. Consequently, the proposed method enables us to optimize the RPM imaging parameters using only the observation data, namely, automatic parameter selection can be achieved. The numerical tests, using the three-dimensional simplified human body model, demonstrate that our proposed method maintains the most accurate results without manually or empirically parameter adjustment.

## II. SYSTEM MODEL

Figure 1 shows a representative observation model, assumed in this study. Several transmitters and receivers are arranged on the plane  $y = 0$ , and the locations of the transmitter and receiver are defined as  $\mathbf{L}_T = (X_T, 0, Z_T)$  and  $\mathbf{L}_R = (X_R, 0, Z_R)$ , respectively. At each combination, an electric field is recorded as  $\tilde{s}(\mathbf{L}_T, \mathbf{L}_R, R)$ , where  $R = ct/2$ ,  $t$  is the time, and  $c$  is the speed of light. The output of the range extraction filter (*e.g.*, matched filter) is defined as  $s(\mathbf{L}_T, \mathbf{L}_R, R)$ . Here, we introduce a set of discrete points as  $\mathbf{q} \equiv (\mathbf{L}_T, \mathbf{L}_R, R)$ , so-called range point, which are extracted by the local maxima of  $|s(\mathbf{L}_T, \mathbf{L}_R, R)|$  as to  $R$ .

## III. ORIGINAL RPM METHOD

Here, we briefly describe the methodology of the RPM method, which is one of the most accurate and lowest complexity 3-D imaging algorithm. The RPM is based on incoherent mapping from each range point  $\mathbf{q}_i$  to its solely associated scattering center  $\mathbf{p}(\mathbf{q}_i)$  via the weighted kernel density estimator as

$$\hat{\mathbf{p}}(\mathbf{q}_i) = \arg \max_{\mathbf{p}^{\text{int}}(\mathbf{q}_i; \mathbf{q}_j, \mathbf{q}_m) \in \mathcal{P}_i} \sum_{\mathbf{q}_j, \mathbf{q}_k \in \mathcal{Q}_i} g(\mathbf{q}_i; \mathbf{q}_j, \mathbf{q}_k) \times \exp \left[ -\frac{\|\mathbf{p}^{\text{int}}(\mathbf{q}_i; \mathbf{q}_j, \mathbf{q}_k) - \mathbf{p}^{\text{int}}(\mathbf{q}_i; \mathbf{q}_l, \mathbf{q}_m)\|^2}{2\sigma_r^2} \right] \quad (1)$$

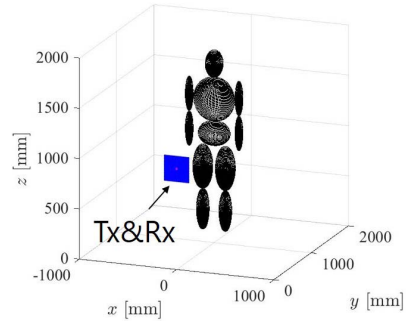


Fig. 1. Observation model. Planar arrays are located to human body target.

where  $\mathbf{p}^{\text{int}}(\mathbf{q}_i; \mathbf{q}_l, \mathbf{q}_m)$  denotes the intersection point of three spheroids determined by  $\mathbf{q}_i$ ,  $\mathbf{q}_l$ , and  $\mathbf{q}_m$ , and  $\sigma_r$  determines the standard deviation of the Gaussian function and is empirically given according to prior knowledge.  $\mathcal{P}_i$  denotes a set of all possible intersection points.  $\mathcal{Q}_i$  denotes a set of range points except for  $\mathbf{q}_i$ . The weight function  $g(\mathbf{q}_i; \mathbf{q}_j, \mathbf{q}_k)$  is defined as:

$$g(\mathbf{q}_i; \mathbf{q}_j, \mathbf{q}_k) = |s(\mathbf{q}_j)| \exp \left[ -\frac{D(\mathbf{q}_i, \mathbf{q}_j)^2}{2\sigma_D^2} \right] + |s(\mathbf{q}_k)| \exp \left[ -\frac{D(\mathbf{q}_i, \mathbf{q}_k)^2}{2\sigma_D^2} \right] \quad (2)$$

where  $|s(\mathbf{q}_j)|$  is the value of the local maxima of  $|s(\mathbf{L}_{T,j}, \mathbf{L}_{R,j}, R_j)|$ , and  $D(\mathbf{q}_i, \mathbf{q}_j)$  refers to the three-dimensional Euclidean distance between the sensors of  $\mathbf{q}_i$  and  $\mathbf{q}_j$ . Although the accuracy in RPM imaging largely depends on the selected parameters of  $\sigma_D$  and  $\sigma_r$ , these parameters are empirically selected in the original RPM algorithm.

## IV. PROPOSED RPM

### A. GMM Model for Estimating Direction of Arrival (DOA)

To automatically determine the parameters in RPM, we introduced the GMM-based probabilistic density function estimator and simultaneously optimized their hyperparameters via the EM algorithm. In this section, we introduce the GMM-based estimation of the DOA for each RP  $\mathbf{q}_i$ . By assuming a 3-D model, the PDF for the elevation and azimuth angles  $(\theta, \phi)$  for  $\mathbf{q}_i$  is modeled as:

$$P(\theta, \phi; \mathbf{q}_i) \equiv \sum_{\mathbf{q}_j, \mathbf{q}_k \in \mathcal{Q}_i} \delta(\theta - \theta_{i,j,k}, \phi - \phi_{i,j,k}) \times G(\mathbf{q}_i; \mathbf{q}_j, \mathbf{q}_k) \quad (3)$$

where  $\delta(\theta, \phi)$  expresses the two-dimensional (2-D) Dirac's delta function.  $G(\mathbf{q}_i; \mathbf{q}_j, \mathbf{q}_k) \equiv g(\mathbf{q}_i; \mathbf{q}_j, \mathbf{q}_k) / \sum g(\mathbf{q}_i; \mathbf{q}_j, \mathbf{q}_k)$  denotes the weight function, where  $g(\mathbf{q}_i; \mathbf{q}_j, \mathbf{q}_k)$  is defined in Eq. (2).  $\theta_{i,j,k}$  and  $\phi_{i,j,k}$  denote the elevation and azimuth angles, respectively, which were determined by the intersection point of  $\mathbf{p}^{\text{int}}(\mathbf{q}_i; \mathbf{q}_j, \mathbf{q}_k)$  according to the following relationship:

$$\mathbf{p}^{\text{int}}(\mathbf{q}_i; \mathbf{q}_j, \mathbf{q}_k) = \begin{pmatrix} R_i \cos \theta_{i,j,k} \cos \phi_{i,j,k} \\ R_i \sin \theta_{i,j,k} \cos \phi_{i,j,k} \\ R_i \sin \theta_{i,j,k} \end{pmatrix}^T \quad (4)$$

Thus, the determination of the scattering center  $\hat{p}(\mathbf{q}_i)$  in Eq. (1) is equivalent to optimizing a set of  $\theta$  and  $\phi$  from the corrections of  $\theta_{i,j,k}$  and  $\phi_{i,j,k}$ . Here, this method determines the optimal set of  $(\theta, \phi)$  for each  $\mathbf{q}_i$  by using the following maximum likelihood (ML) estimate as  $P(\theta, \phi, \mathbf{q}_i)$  with the GMM model as:

$$(\hat{\theta}_{\text{ML}}(\mathbf{q}_i), \hat{\phi}_{\text{ML}}(\mathbf{q}_i)) = \arg \max_{(\theta, \phi)} \sum_{k=1}^K \pi_k \mathcal{N}(\theta, \phi | \mu_k, \Sigma_k) \quad (5)$$

where  $\pi_k$  denotes the weight, and  $\mathcal{N}(\theta, \phi | \mu_k, \Sigma_k)$  denotes the 2-D Gaussian distribution with the mean  $\mu_k$  and the covariance matrix  $\Sigma_k$ . Subsequently, the parameter optimization problems of  $\sigma_r$  in Eq. (1) could be converted to those for optimizing the covariance values in the GMM model denoted as  $\Sigma_k$ .

### B. EM Algorithm for $\sigma_r$ Optimization

To solve the optimization in Eq. (5), we used the EM algorithm in the Bayesian framework, and the set of hyper parameters as  $(\mathbf{M}, \Sigma)$  are simultaneously optimized with the ML solution, where  $\mathbf{M} \equiv (\mu_1, \mu_2, \dots, \mu_K)$  and  $\Sigma \equiv (\Sigma_1, \Sigma_2, \dots, \Sigma_K)$ . Here, we briefly describes the EM algorithm, which recursively conducts the following E and M steps. Introducing  $\Theta \equiv (\theta_1, \dots, \theta_N)$  and  $\Phi \equiv (\phi_1, \dots, \phi_N)$ ,  $\mathbf{X} = (\Theta, \Phi)$  set as the observed data and  $\mathbf{Z}$  as the unobserved latent data, the ML estimate is determined by maximizing the following marginal likelihood  $L(\mathbf{M}, \Sigma)$  as:

$$L(\mathbf{M}, \Sigma) = \int p(\mathbf{X}, \mathbf{Z} | \mathbf{M}, \Sigma) d\mathbf{Z} \quad (6)$$

The EM algorithm iteratively finds the ML estimate by the following two steps:

Let  $\mathbf{M}^{(n)}$  and  $\Sigma^{(n)}$  be the estimates of  $\mathbf{M}$  and  $\Sigma$ , respectively, at the  $n$ -th iteration. E step): Taking the expectation value of the log likelihood function as:

$$Q(\mathbf{M}^{(n)}, \Sigma^{(n)}) = \sum_{\mathbf{Z}} p(\mathbf{Z} | \mathbf{M}^{(n)}, \Sigma^{(n)}) \times \log p(\mathbf{X}, \mathbf{Z} | \mathbf{M}^{(n)}, \Sigma^{(n)}) \quad (7)$$

M step): Determining the hyper parameters maximizing the following functions as:

$$(\mathbf{M}^{(n+1)}, \Sigma^{(n+1)}) = \arg \max_{(\mathbf{M}, \Sigma)} Q(\mathbf{M}, \Sigma | \mathbf{M}^{(n)}, \Sigma^{(n)}) \quad (8)$$

Then, we obtain the ML estimate of the DOA of  $(\hat{\theta}_{\text{ML}}(\mathbf{q}_i), \hat{\phi}_{\text{ML}}(\mathbf{q}_i))$  in Eq. 5 with optimized hyper parameters  $(\hat{\mathbf{M}}, \hat{\Sigma})$ . Figure 2 shows the schematic image in converting the corrected samples to the PDF with GMM model and EM algorithm. It is noteworthy that the optimized hyper parameters  $\hat{\Sigma}$  should be equivalent to the  $\sigma_r$  parameter introduced in Eq. (1), which is invariant to the selected range point  $\mathbf{q}_i$ . Thus, the proposed scheme, but can offer an appropriate parameter for each range point  $\mathbf{q}_i$ , which has been determined by the stochastic profiles of the distribution of  $(\Theta, \Phi)$ .

### C. Optimization of $\sigma_D$ by $k$ -Space Data Decomposition

While the above GMM and EM scheme provides the optimization of  $\sigma_r$  in Eq. (1),  $\sigma_D$  still needs to be determined to calculate  $G(\mathbf{q}_i; \mathbf{q}_j, \mathbf{q}_k)$  in Eq. (2). Here, we introduce  $\sigma_D$

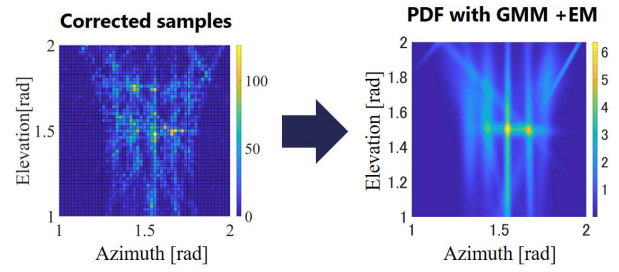


Fig. 2. PDF generation by GMM and EM algorithm.

scheme by exploiting the  $k$ -space decomposition algorithm as in [23]. First, the methodology for  $k$ -space decomposition in the RPM scheme is briefly described as follows. Focusing on one transmitter, the planar array or scanning on the  $y = 0$  plane is assumed, each receiver location is redefined as  $\mathbf{L}_R \equiv (X, 0, Z)$  and the output of the range extraction filter is also redefined as  $s(X, Z, R; \mathbf{L}_T)$ . Then, the 2-D Fourier transform converts the data  $s(X, Z, R; \mathbf{L}_T)$  to  $k_{x,z}$ -space as:

$$S(k_x, k_z, R; \mathbf{L}_T) = \int_{\mathbf{L}_R \in \Omega} s(X, Z, R; \mathbf{L}_T) e^{-j(k_x X + k_z Z)} dX dZ, \quad (9)$$

where  $\Omega$  denotes the area of the receiver array. Next, the  $k$  associated range points are extracted as  $\mathbf{q}_m^k \equiv (k_{x,m}, k_{z,m}, R_m)$ :

$$\left. \begin{aligned} \partial |S(k_x, k_z, R; \mathbf{L}_T)| / \partial k_x &= 0 \\ \partial |S(k_x, k_z, R; \mathbf{L}_T)| / \partial k_z &= 0 \\ \partial |S(k_x, k_z, R; \mathbf{L}_T)| / \partial R &= 0 \end{aligned} \right\}. \quad (10)$$

The decomposition in the  $k_x$  and  $k_z$  spaces is equivalent to that in the elevation and azimuth angle of arrival. This method has a definitive advantage that it could decompose the multiple responses from multiple targets within the same gate range and offers robustness against noise owing to the coherent integration process, compared with other super-range resolution techniques, such as Capon, MUSIC, and CS, which has been demonstrated in [23]. In addition, the responses in  $k_x$ - $k_z$  space reveal significant information to determine  $\sigma_D$  in the sequential RPM process. Figure 3 shows the relationship between various curvature targets and  $k$ -space responses, indicating that the  $k$ -space responses become narrower in the case of a large plate, namely, the infinite radius of curvature, and in the case of a point target, *i.e.*, nearly zero radius of curvature, its response becomes wider. In addition, Fig. 4 shows the relationship between the target with small and large curvature radii and scattering center points, indicating that  $\sigma_D$  should be a smaller in the case of smaller curvature radius, because the scattering center would be closely located to the intersection points depicted by the two circles, and vice versa. According to the above discussion, we determine an appropriate  $\sigma_D$  for each axis  $X$  and  $Z$ , denoted as  $\sigma_{D_X}$  and  $\sigma_{D_Z}$ , based on the  $k$ -space responses according to the following equation:

$$\hat{\sigma}_{D_X}(\mathbf{q}_m^k) = \frac{|\Delta k_{\max} - \Delta k_{\min}|}{|\Delta k_x(\mathbf{q}_m^k) - \Delta k_{\min}|} \quad (11)$$

$$\hat{\sigma}_{D_Z}(\mathbf{q}_m^k) = \frac{|\Delta k_{\max} - \Delta k_{\min}|}{|\Delta k_z(\mathbf{q}_m^k) - \Delta k_{\min}|} \quad (12)$$

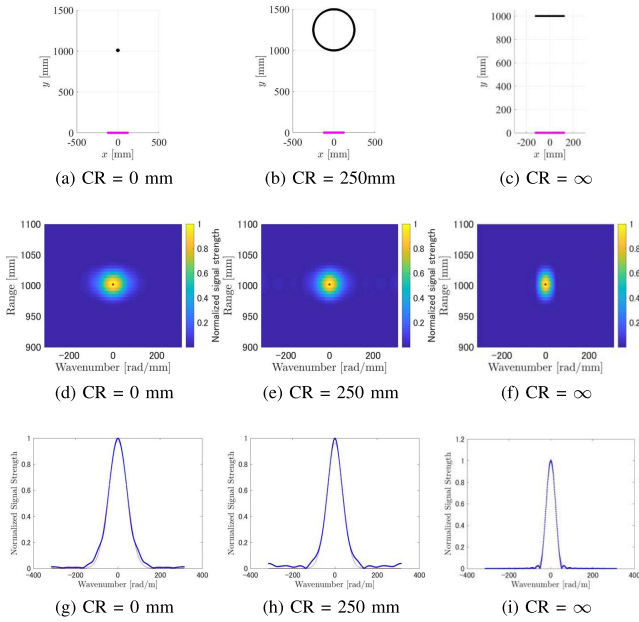


Fig. 3. Relationship between target size (curvature radius (CR)) and  $k$ -space profile. (a)-(c): Observation model. (d)-(f): Range- $k$  space profile. (g)-(i): Cross-sectional  $k$ -space image at the distance of 1000 mm.

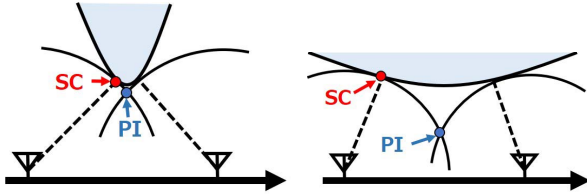


Fig. 4. Relationship between curvature radius and  $k$ -space profile. PI denotes the point of intersection of two spheres depicted by  $q_i$  and  $q_j$ . SC denotes the scattering center point associated with  $q_i$ .

where  $\Delta k_x(\mathbf{q}_m^k)$  and  $\Delta k_z(\mathbf{q}_m^k)$  denote the spread value of  $|S(k_x, k_z, R; \mathbf{L}_T)|$  with the center of  $\mathbf{q}_m^k$  along the  $k_x$  and  $k_z$  axes, respectively. Moreover,  $\Delta k_{\min}$  and  $\Delta k_{\max}$  indicate the spread value in the  $k$ -space assuming the point target (CR = 0 mm) and plate target (CR =  $\infty$ ), as shown in Fig. 3.

Finally, for each extracted  $k$ -space associated range point as  $\mathbf{q}_m^k$ , the GMM based RPM converts its scattering center point as  $\hat{\mathbf{p}}(\mathbf{q}_m^k)$ , where  $g(\mathbf{q}_i; \mathbf{q}_j, \mathbf{q}_k)$  used in Eq. (2) is updated as:

$$\begin{aligned} & \tilde{g}(\mathbf{q}_i^k; \mathbf{q}_j^k, \mathbf{q}_k^k) \\ &= +s(\mathbf{q}_j^k) \left( \exp \left[ -\frac{D_X(\mathbf{q}_i^k, \mathbf{q}_j^k)^2}{2\hat{\sigma}_{D_X}(\mathbf{q}_i^k)^2} \right] + \exp \left[ -\frac{D_Z(\mathbf{q}_i^k, \mathbf{q}_j^k)^2}{2\hat{\sigma}_{D_Z}(\mathbf{q}_i^k)^2} \right] \right) \\ &+ s(\mathbf{q}_k^k) \left( \exp \left[ -\frac{D_X(\mathbf{q}_i^k, \mathbf{q}_k^k)^2}{2\hat{\sigma}_{D_X}(\mathbf{q}_i^k)^2} \right] + \exp \left[ -\frac{D_Z(\mathbf{q}_i^k, \mathbf{q}_k^k)^2}{2\hat{\sigma}_{D_Z}(\mathbf{q}_i^k)^2} \right] \right) \end{aligned} \quad (13)$$

where  $D_X(\mathbf{q}_i, \mathbf{q}_j)$  and  $D_Z(\mathbf{q}_i, \mathbf{q}_j)$  denote the Euclidean distance between the sensor locations in  $\mathbf{q}_i$  and  $\mathbf{q}_j$  along the  $x$  and  $z$  axes, respectively. Using this method,  $\sigma_{D_X}$  and  $\sigma_{D_Z}$  can be automatically determined by the profile of  $|S(k_x, k_z, R; \mathbf{L}_T)|$ .

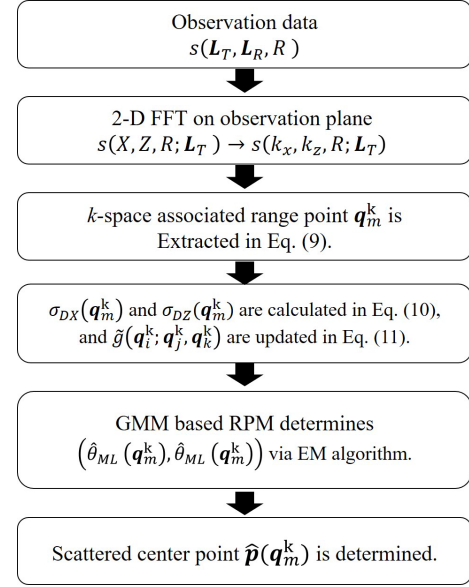


Fig. 5. Flowchart of the proposed method.

#### D. Procedure of Proposed Method

The procedure of the proposed method can be summarized as follows.

- Step 1) The observed data recorded at each transmitter and receiver combination, is processed by range extraction filter, and  $s(\mathbf{L}_T, \mathbf{L}_R, R)$  is acquired.
- Step 2) For each  $\mathbf{L}_T$ ,  $s(X, Z, R; \mathbf{L}_T)$  is converted to  $S(k_x, k_z, R; \mathbf{L}_T)$  in Eq. (9) and  $\mathbf{q}_m^k$  is extracted from Eq. (10).
- Step 3)  $\hat{\sigma}_{D_X}(\mathbf{q}_m^k)$  and  $\hat{\sigma}_{D_Z}(\mathbf{q}_m^k)$  are determined in Eq. (11), and  $\tilde{g}(\mathbf{q}_i^k; \mathbf{q}_j^k, \mathbf{q}_k^k)$  is updated in Eq. (13).
- Step 4) For each  $\mathbf{q}_m^k$ ,  $(\hat{\theta}_{ML}(\mathbf{q}_m^k), \hat{\phi}_{ML}(\mathbf{q}_m^k))$  is determined in Eq. (5), namely, the GMM based RPM is applied, where a hyper parameter set  $\boldsymbol{\mu}_k$  and  $\boldsymbol{\Sigma}_k$  are automatically determined by the EM algorithm. Then, its scattering center point is calculated as

$$\hat{\mathbf{p}}(\mathbf{q}_m^k) \equiv \begin{pmatrix} R_m \cos \hat{\theta}_{ML}(\mathbf{q}_m^k) \cos \hat{\phi}_{ML}(\mathbf{q}_m^k) \\ R_m \sin \hat{\theta}_{ML}(\mathbf{q}_m^k) \cos \hat{\phi}_{ML}(\mathbf{q}_m^k) \\ R_m \sin \hat{\phi}_{ML}(\mathbf{q}_m^k) \end{pmatrix}^T$$

Figure 5 shows the procedure of the proposed method.

### V. NUMERICAL TESTING

#### A. Numerical Setting

In this section, the 3-D numerical tests are demonstrated to validate the effectiveness of our method. Figure 1 also shows the simulation model, where a human body target is composed of 11 ellipsoids. Note that, this simulation model is introduced in numerous studies [18], [23]. This model enables us to assess an imaging result in a strictly quantitative manner, which is hardly obtained from a real human body [20]. The transmitted source current forms a pulse modulated sinusoidal wave with a center frequency of 20.0 GHz (wavelength, 15mm) and bandwidth of 3.0 GHz (range resolution, 50 mm). Since we assume the MMW radar system, reflection data are generated via geometrical optics (GO) approximation [24], namely,

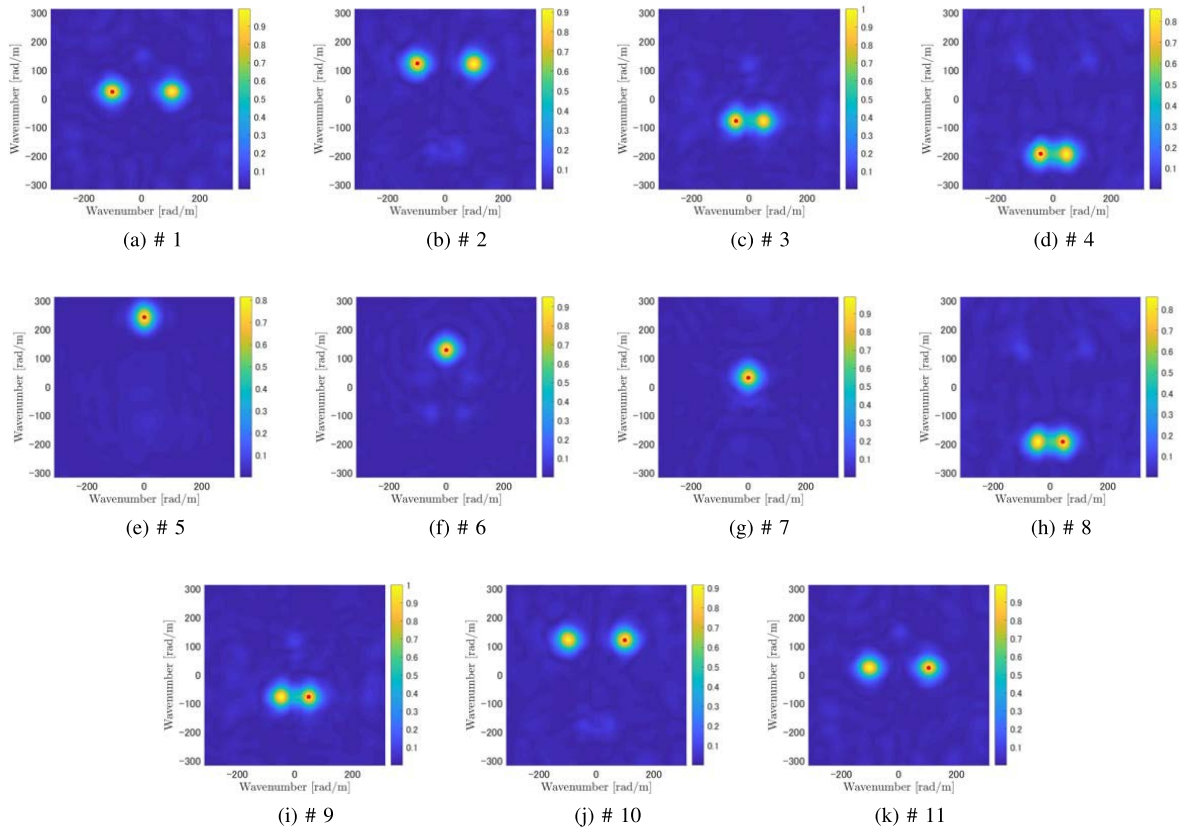


Fig. 6.  $k$ -space profiles at each distinguished range. Red denotes the extracted point as  $(\tilde{k}_{x,m}, \tilde{k}_{z,m}, \tilde{R}_m)$ .

the ray-tracing method, because we deal with an object whose size is considerably larger than the wavelength of the MMW band. The GO is known as one of the most promising forward solvers for the high-frequency electromagnetic propagation model, where each propagation path is calculated by the law of reflection with propagation loss. Nonetheless, in the GO analysis, an interference effect among multiple objects is considered, while the effect of multiple scattering is ignored. Here, the SIMO model is introduced, and  $25 \times 25$  receivers with  $2/3$  wavelength arranged on the  $y = 0$  plane are defined with a spacing of 10 mm. One transmitter is located at the center of this planar array, as shown in Fig. 1. To assess the noise-robustness of each method, the Gaussian white noise is added to a received signal in the time domain, and the S/N ratio is defined as the ratio of the instantaneous peak signal power of the data to the average noise power.

### B. Case in the Absence of Noise

First, we tested the reconstruction performances in a noise-free situation to assess the systematic error of each method. Figure 6 shows the number of  $k$ -space profiles at each range and extracted the  $k$  associated range points  $\mathbf{q}_m^k$  in Eq. 10. This figure demonstrates that the  $k$ -space decomposition approach separates responses from 11 ellipsoid objects and contributes obtaining a highly accurate profile of range points, as shown in Fig. 7. Figure 8 shows the reconstruction results obtained by the method reported in [23] and the proposed method. Note that the method presented in [23] uses

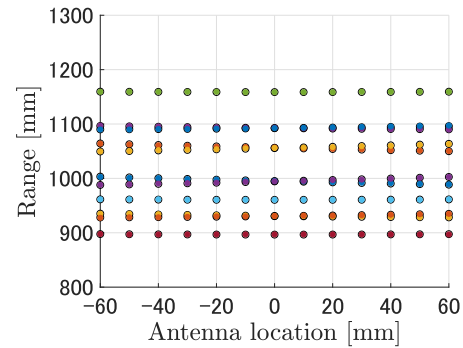


Fig. 7. Extracted range points profile after  $k$ -space decomposition. Each color of dots present a clustered number in  $k$ -space.

the RPM algorithm denoted in Eqs. (1) and (2), assuming that  $\sigma_r = 1$  mm and  $\sigma_D = 30$  mm. This figure shows that this method offers a certain level of reconstruction accuracy due to the  $k$ -space decomposition, but fluctuations occur for each body part in the RPM reconstruction points,  $\hat{\mathbf{p}}(\mathbf{q}_i)$ . While this fluctuation could be suppressed by changing the parameters  $\sigma_r$  and  $\sigma_D$ , it is impractical to determine an optimal combination of these parameters at the initial stage without prior knowledge of the target shape or distribution, which is the main issue discussed in this study. On the contrary, the proposed method shown in Fig. 8 offers a more accurate reconstruction image by introducing the GMM and EM algorithm based parameter optimization for  $\sigma_r$  and  $k$ -space profile based determination of  $\sigma_{D_X}$  and  $\sigma_{D_Z}$ . Here, the number of Gaussian kernels denoted

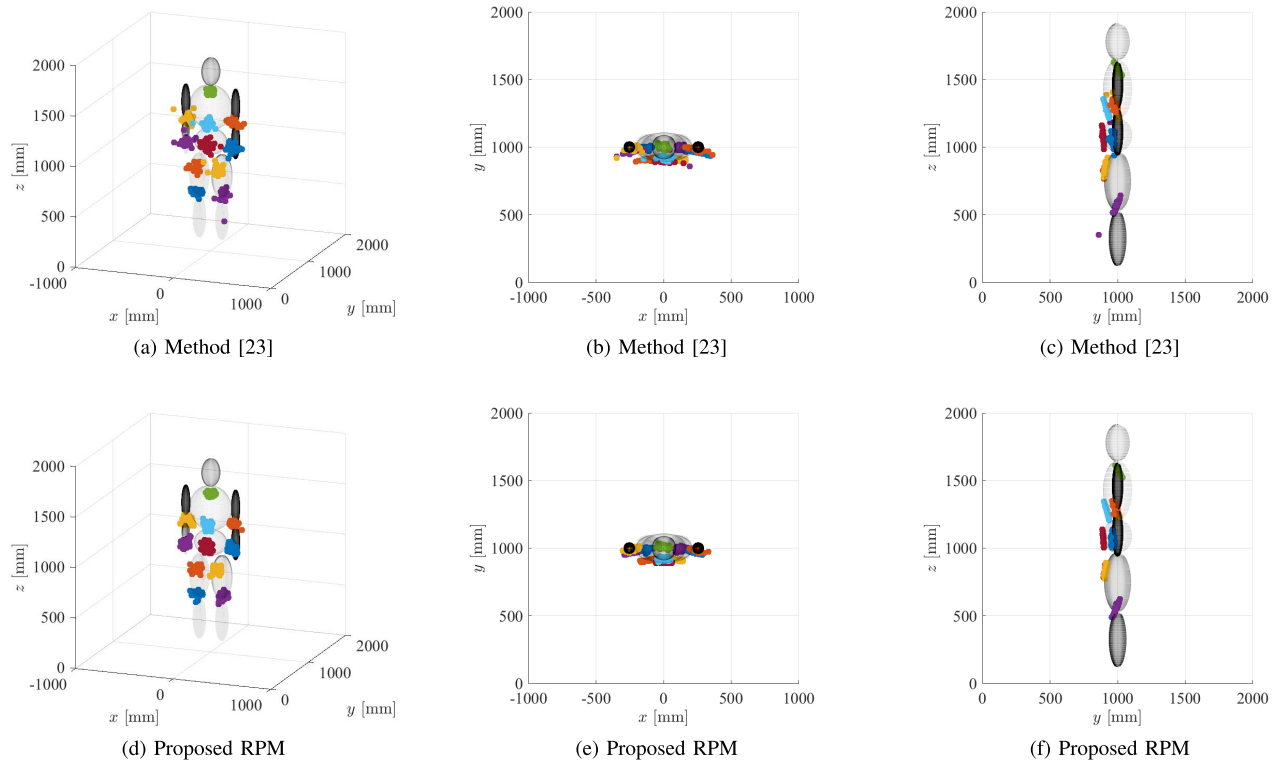


Fig. 8. Reconstruction results obtained by the method [23] and the proposed method, at  $S/N = \infty$ .

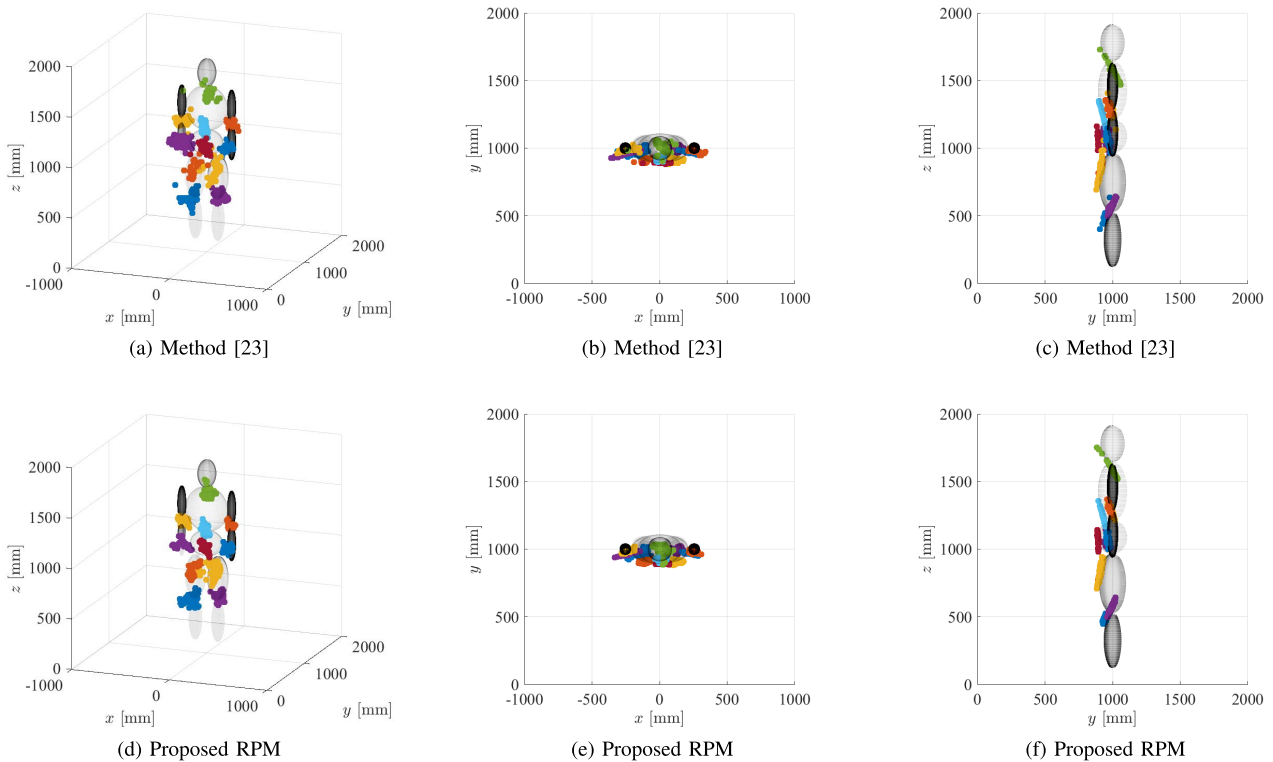


Fig. 9. Reconstruction results obtained by the method [23] and the proposed method, at  $S/N = 5$  dB.

as  $K$  in Eq. (5) is set to 200. Notably, the computational times of the method [23] and proposed method are 250 s and 730 s, respectively, using an Intel(R) Xeon(R) Silver 4110 CPU @

2.10GHz with 128 GB RAM. However, the proposed method required additional computational expenses, particularly with respect to optimization of the hyper parameters for each range

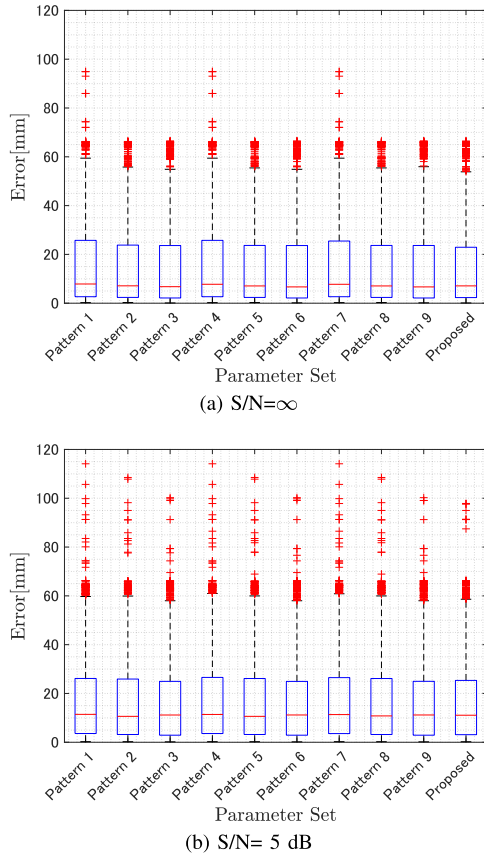


Fig. 10. Box plots for reconstruction accuracy of the RPM imaging at each S/N level. Red line denotes the median. Upper and lower boundaries denote lower and upper quartile, respectively. Upper and lower whiskers denote maximum and minimum values, respectively. Red cross points are outlier over the whiskers.

point. It is possible to reduce these costs, *e.g.*, by decreasing the number of Gaussian kernels or samples in the GMM generations.

### C. Case in the Presence of Noise

The above effect is clearer in a noisy situation. Here, we tested a low signal-to-noise (SNR) ratio as  $S/N = 5$  dB. Here, SNR is defined as the ratio of peak intensity to the average noise power of a signal recorded in the time domain, *i.e.*, data before the Doppler or RMA processing. These SNRs for all transmitter and receiver combinations are averaged. Moreover, SNR is defined at each slow time and not related to a coherent integration process along the slow time or the aperture array. Figure 9 shows the reconstruction results for each method in this SNR case. The method used in [23] uses  $\sigma_r = 1$  mm and  $\sigma_D = 30$  mm, which is the same in the noiseless case. These results demonstrated that the exiting method in [23] suffers from inaccuracy due to random noise, and image fluctuations are more critical compared to noise-free situation. However, the proposed method maintains its accuracy even in this case, because the GMM and EM algorithm could dynamically change an appropriate parameter about  $\sigma_r$ . Note that, the proposed method determines a different optimized parameter set as  $\mu_k, \Sigma_k$  for each range point, which is constant in the method used in [20].

TABLE I  
PARAMETER SETS FOR EACH CASE IN THE METHOD [23]

	$\sigma_D=10$ mm	$\sigma_D=30$ mm	$\sigma_D=100$ mm
$\sigma_r=1$ mm	Pattern 1	Pattern 2	Pattern 3
$\sigma_r=10$ mm	Pattern 4	Pattern 4	Pattern 6
$\sigma_r=100$ mm	Pattern 7	Pattern 8	Pattern 9

TABLE II  
CLUSTERING INDEXES FOR EACH PART OF HUMAN BODY

Index	Part	Index	Part
# 1	Lower right arm	# 7	Torso
# 2	Upper right arm	# 8	Lower left leg
# 3	Upper right leg	# 9	Upper left leg
# 4	Lower right leg	# 10	Upper left arm
# 5	Head	# 11	Lower left arm
# 6	Breast		

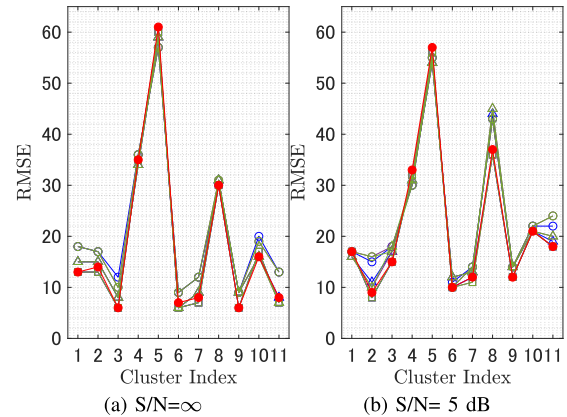


Fig. 11. RMSE plots for each part of human body at each S/N level. Red dots denote the proposed method. The colors of blue, purple, and green denote the case of  $\sigma_D = 10$  mm,  $\sigma_D = 30$  mm, and  $\sigma_D = 240$  mm, respectively. The mark types of triangle, square, circles denote the case of  $\sigma_D = 1$  mm,  $\sigma_D = 10$  mm, and  $\sigma_D = 100$  mm, respectively.

### D. Quantitative Error Analysis

As a statistical error analysis, Fig. 10 illustrates the box plot of the reconstruction errors in the RPM imaging results at each SNR level. Here, nine combination patterns of  $\sigma_r$  and  $\sigma_D$  in the method [23] were investigated, where each parameter set is summarized in Table I. The reconstruction error, namely the vertical axis in Fig. 10, is defined as the minimum distance between each true ellipsoidal boundary and reconstruction point,  $\hat{p}(q_i)$ . The lower and upper bounds of the boxes spanned the interquartile range (IQR). The lower and upper whiskers indicate the  $\pm 2.7$  standard deviation range, while the red crosses, in Fig. 10, were regarded as outliers. Figure 10 shows that the selected parameters determine the outcomes in the method [23]. Furthermore, inappropriate selection of these parameters generates significant outliers (the red crosses in Fig. 10), particularly in the case of 1, 4, and 7, both in noiseless and noisy situations. Conversely, the proposed method offered the same level of accuracy as that obtained in case 3, which was the most accurate result in the method [23]. Notable, compared with other cases, the proposed method reduced the number of outliers using only the observed data without the requirement for prior knowledge or empirical testing. In addition, we investigate the error analysis for each part of human body, which are separately reconstructed by the  $k$ -space decomposition. Table II indicates clustering indexes

for 11 ellipsoidal part of human body. Figure 11 shows the RMSEs for each body part, where the 9 types of parameter combination as in Table I are investigated in the method [23]. This figure also demonstrates that our proposed method retains lowest RMSEs for most parts of human body, and revealed that our method provides an optimal performance of the RPM method without using a prior knowledge or empirically selections of the parameters.

## VI. CONCLUSION

We introduced a data-driven parameter optimization scheme for 3-D short-range radar imaging using the unique feature of the RPM imaging and  $k$ -space decomposition. The accuracy of the existing RPM method like [20], [23] has an inherent problem that its accuracy significantly depends on the selected parameters, which are usually empirically determined. Thus, the proposed method introduced the automatic optimization scheme using EM algorithm-based hyperparameter optimization, where the distribution of intersection points is modeled by the GMM. The optimal azimuth and elevation angles of the reflection point are determined by the MLEM framework, and the mean and variances of each Gaussian distribution are simultaneously determined, indicating that our method individually selects the optimization parameter for each range point. In addition, by focusing on the relationship between the  $k$ -space profile and curvature radius of the target shape,  $\sigma_D$  is analytically determined by  $k$ -space responses. The GO-based numerical tests, assuming the MMW SIMO radar system, demonstrated that our proposed method retains a maximum performance of the 3-D image reconstruction, which is the same level as that obtained by the method used in [23] with manually tuned parameters. This approach can be extended to other similar problems, such as Doppler velocity estimation in [25]. Furthermore, the numerical test assumes a short-range scenario where the distance from the radar to human body is 1 m, while assuming the wavelength of the transmitted pulse as 15 mm; it is a completely far-field scenario. Considering a more far-field situation required for automotive radar, such as 5 or 10 m, the aperture angle becomes smaller with the same 2-D array size, and the range points accumulate more intensively within the range resolutions, compared with the case in Fig. 7. Thus, the original or proposed RPM is subject to range point errors owing to the interference effect, even when using  $k$ -space decomposition. Regarding parameter optimization, assuming a farther-field case, the actual scattering center may accumulate at a representative reflection point of each human body, *i.e.*, this needs to handle objects with high curvature. Therefore, the sensitivity of the selected parameters of  $\sigma_D$  or  $\sigma_r$  is more remarkable in the original RPM. In contrast, the proposed RPM takes into account the  $k$ -space responses or cumulative degree of intersection points to determine the appropriate parameters of the GMM model,  $\sigma_{D_x}$ , or  $\sigma_{D_y}$  and mitigate the RPM imaging errors, even in far-field cases. The above mentioned investigation will be our important future work.

## REFERENCES

- [1] J. A. Nanzer and R. L. Rogers, "Human presence detection using millimeter-wave radiometry," *IEEE Trans. Microw. Theory Techn.*, vol. 55, no. 12, pp. 2727–2734, Dec. 2007.
- [2] M. Vahidpour and K. Sarabandi, "Millimeter-wave Doppler spectrum and polarimetric response of walking bodies," *IEEE Trans. Geosci. Remote Sens.*, vol. 50, no. 7, pp. 2866–2881, Jul. 2012.
- [3] X. Huang, J. Ding, D. Liang, and L. Wen, "Multi-person recognition using separated micro-Doppler signatures," *IEEE Sensors J.*, vol. 20, no. 12, pp. 6605–6611, Jun. 2020.
- [4] R. Du, Y. Fan, and J. Wang, "Pedestrian and bicyclist identification through micro Doppler signature with different approaching aspect angles," *IEEE Sensors J.*, vol. 18, no. 9, pp. 3827–3835, May 2018.
- [5] D. A. Andrews, S. W. Harmer, N. J. Bowring, N. D. Rezgui, and M. J. Southgate, "Active millimeter wave sensor for standoff concealed threat detection," *IEEE Sensors J.*, vol. 13, no. 12, pp. 4948–4955, Dec. 2013.
- [6] L. Ding, S. Wu, P. Li, and Y. Zhu, "Millimeter-wave sparse imaging for concealed objects based on sparse range migration algorithm," *IEEE Sensors J.*, vol. 19, no. 16, pp. 6721–6728, Aug. 2019.
- [7] B. Gonzalez-Valdes, Y. Alvarez, S. Mantzavinos, C. M. Rappaport, F. Las-Heras, and J. A. Martinez-Lorenzo, "Improving security screening: A comparison of multistatic radar configurations for human body imaging," *IEEE Antennas Propag. Mag.*, vol. 58, no. 4, pp. 35–47, Apr. 2016.
- [8] F. Soldovieri, A. Brancaccio, G. Prisco, G. Leone, and R. Pierri, "A Kirchhoff-based shape reconstruction algorithm for the multi-monostatic configuration: The realistic case of buried pipes," *IEEE Trans. Geosci. Remote Sens.*, vol. 46, no. 10, pp. 3031–3038, Oct. 2008.
- [9] H. Sun, C. Gao, Z. Zhang, X. Liao, X. Wang, and J. Yang, "High-resolution anisotropic prestack kirchhoff dynamic focused beam migration," *IEEE Sensors J.*, vol. 20, no. 20, pp. 11753–11760, Oct. 2020.
- [10] J. M. Lopez-Sahcnez and J. Fortuny-Guasch, "3-D radar imaging using range migration techniques," *IEEE Trans. Antennas Propag.*, vol. 48, no. 5, pp. 728–737, May 2000.
- [11] Z. Wang, Q. Guo, X. Tian, T. Chang, and H.-L. Cui, "Near-field 3-D millimeter-wave imaging using MIMO RMA with range compensation," *IEEE Trans. Microw. Theory Techn.*, vol. 67, no. 3, pp. 1157–1166, Mar. 2019.
- [12] S. S. Ram and A. Majumdar, "High-resolution radar imaging of moving humans using Doppler processing and compressed sensing," *IEEE Trans. Aerosp. Electron. Syst.*, vol. 51, no. 2, p. 1279–1287, Apr. 2015.
- [13] M. Becquaert, E. Cristofani, B. Lauwens, M. Vandewal, J. H. Stiens, and N. Deligiannis, "Online sequential compressed sensing with multiple information for through-the-wall radar imaging," *IEEE Sensors J.*, vol. 19, no. 11, pp. 4138–4148, Jun. 2019.
- [14] R. H. Stolt, "Migration by Fourier transform," *Geophysics*, vol. 43, no. 1, p. 23–48, Feb. 1978.
- [15] L. Zhang, J. Sheng, M. Xing, Z. Qiao, T. Xiong, and Z. Bao, "Wavenumber-domain autofocusing for highly squinted UAV SAR imagery," *IEEE Sensors J.*, vol. 12, no. 5, pp. 1574–1588, May 2012.
- [16] S. Kidera, T. Sakamoto, and T. Sato, "Accurate UWB radar three-dimensional imaging algorithm for a complex boundary without range point connections," *IEEE Trans. Geosci. Remote Sens.*, vol. 48, no. 4, pp. 1993–2004, Apr. 2010.
- [17] T. Sakamoto, T. Sato, P. Aubry, and A. Yarovoy, "Fast imaging method for security systems using ultrawideband radar," *IEEE Trans. Aerosp. Electron. Syst.*, vol. 52, no. 2, pp. 658–670, Apr. 2016.
- [18] Y. Sasaki, F. Shang, S. Kidera, T. Kirimoto, K. Saho, and T. Sato, "Three-dimensional imaging method incorporating range points migration and Doppler velocity estimation for UWB millimeter-wave radar," *IEEE Geosci. Remote Sens. Lett.*, vol. 14, no. 1, pp. 122–126, Jan. 2017.
- [19] S. Takahashi and S. Kidera, "Acceleration of range points migration based microwave imaging for non-destructive testing," *IEEE Antennas Wireless Propag. Lett.*, vol. 17, no. 4, pp. 702–705, Apr. 2018.
- [20] Y. Akiyama and S. Kidera, "Low complexity algorithm for range-point migration-based human body imaging for multistatic UWB radars," *IEEE Geosci. Remote Sens. Lett.*, vol. 16, no. 2, pp. 216–220, Feb. 2019.
- [21] T. Omori and S. Kidera, "Data driven parameter optimization algorithm for RPM based 3-D radar imaging," in *Proc. IEEE Int. Symp. Antennas Propag. (ISAP)*, Oct. 2019, pp. 1–3.
- [22] H. Watanabe, S. Muramatsu, and H. Kikuchi, "Interval calculation of EM algorithm for GMM parameter estimation," in *Proc. IEEE Int. Symp. Circuits Syst.*, May 2010, pp. 2686–2689.

- [23] Y. Akiyama, T. Omori, and S. Kidera, “ $k$ -space decomposition based three-dimensional imaging with range points migration for millimeter wave radar,” *IEEE Trans. Geosci. Remote Sens.*, early access, doi: [10.1109/TGRS.2020.3029301](https://doi.org/10.1109/TGRS.2020.3029301).
- [24] V. U. Zavorotny and A. G. Voronovich, “Comparison of geometric optics and diffraction effects in radar scattering from steep and breaking waves,” in *Proc. IEEE Int. Geosci. Remote Sens. Symp. (IGARSS)*, Jul. 2007, pp. 1350–1353.
- [25] M. Setsu, T. Hayashi, J. He, and S. Kidera, “Super-resolution Doppler velocity estimation by kernel-based range- $\tau$  point conversions for UWB short-range radars,” *IEEE Trans. Geosci. Remote Sens.*, vol. 58, no. 4, pp. 2430–2443, Apr. 2020.



**Tomoki Ohmori** received the B.E. degree in communication engineering and informatics from The University of Electro-Communications, Tokyo, Japan, in 2019, where he is currently pursuing the M.E. degree with the Graduate School of Informatics and Engineering. His research interests include signal processing and imaging for microwave radar as well as its applications.



**Shuto Takahashi** received the B.E. degree in electrical and electronic engineering and the M.E. degree in informatics and communication engineering from The University of Electro-Communications, Tokyo, Japan, in 2017 and 2019.



**Shouhei Kidera** (Member, IEEE) received the B.E. degree in electrical and electronic engineering and the M.I. and Ph.D. degrees in informatics from Kyoto University, Kyoto, Japan, in 2003, 2005, and 2007, respectively. Since 2009, he has been with the Graduate School of Informatics and Engineering, The University of Electro-Communications, Tokyo, Japan, where he is currently an Associate Professor. In 2016, he stayed at the Cross-Disciplinary Electromagnetics Laboratory, University of Wisconsin-Madison, as a Visiting Researcher. His current research interests include advanced radar signal processing, electromagnetic inverse scattering issue for ultra wideband (UWB) three-dimensional sensor, or bio-medical applications. He is also a Senior Member of the Institute of Electronics, Information, and Communication Engineers of Japan (IEICE), and a member of the Institute of Electrical Engineering of Japan (IEEJ) and the Japan Society of Applied Physics (JSAP). He was a Principal Investigator of the PRESTO Program of Japan Science and Technology Agency (JST) from 2017 to 2021. He was a recipient of the 2012 Ando Incentive Prize for the Study of Electronics, the 2013 Young Scientist's Prize by the Japanese Minister of Education, Culture, Sports, Science and Technology (MEXT), and the 2014 Funai Achievement Award.